MATERIALS SCIENCE

Fatigue in assemblies of indefatigable carbon nanotubes

Nitant Gupta, Evgeni S. Penev, Boris I. Yakobson*

Despite being one of the most consequential processes in the utilization of structural materials, fatigue at the nano- and mesoscale has been marginally explored or understood even for the most promising nanocarbon forms—nanotubes and graphene. By combining atomistic models with kinetic Monte Carlo simulations, we show that a pristine carbon nanotube under ambient working conditions is essentially indefatigable—accumulating no structural memory of prior load; over time, it probabilistically breaks, abruptly. In contrast, by using coarse-grained modeling, we demonstrate that any practical assemblies of nanotubes, e.g., bundles and fibers, display a clear gradual strength degradation in cyclic tensile loading due to recurrence and ratchet-up of slip at the tube-tube interfaces, not occurring under static load even of equal amplitude.

INTRODUCTION

Low-dimensional carbon nanomaterials came to prominence largely because of their remarkable mechanical properties and as potential lower-density replacements of predominant structural materials such as metals and ceramics. Besides strength, a crucial characteristic of these materials is the fatigue (*1*), which is often linked directly to their usable life. Fatigue in three-dimensional (3D) bulk materials is closely related to the propagation and accumulation of structural defects that seem to preexist inadvertently but inevitably. On the contrary, it is now possible to achieve arbitrarily large pristine/perfect low-dimensional carbon forms (*2*). An important question thus arises as to how "fatigue" can be defined for a perfect carbon nanotube (CNT) or graphene and what are the underlying atomistic mechanisms. This remains a challenging problem, and only very recently, attempts have been made toward quantitative measurements of individual CNTs (*3*) and graphene (*4*, *5*).

All credible definitions of materials fatigue explicitly mention cyclic loading (*1*), a repeated application of stresses (load-control) or strains (displacement-control), as a necessary condition. It is asserted that plasticity must be induced in each cycle, arising from dislocation motion, and leading to increase in dislocation density along the so-called persistent slip bands (*6*). This then causes strain localization along these bands, acting as nucleation sites for microcracks. Subsequently, the opening up of these microcracks leads to further stress concentration and eventual failure of the material.

If carbon forms such as CNTs are pristine, defects and microcracks are absent and cannot be formed spontaneously under typical working conditions ($T \lesssim 1500$ K). Moreover, their cyclic loading is restricted to tension-tension mode because CNTs with their high length-to-diameter (L/d) aspect ratio do not sustain compression and will instead buckle with no structural damage (*7*). Under these circumstances, a single cycle at typical frequencies, e.g., ~1 to 1000 Hz, does not provide sufficient time to nucleate a crack or defect, and a tube remains intact even after multiple cycles. As a consequence, over a long time, such a tube should behave no differently than under static loading, and the time scale for crack/defect nucleation should thus be similar. It may be more appropriate to characterize the temporal failure of nanotubes as a form of "creep" failure. However, the experimental studies on the fatigue of pristine carbon forms (*3*, *4*) do use cyclic loading and unanimously term the observed failure as "fatigue failure." It is important to clearly stipulate the underlying failure mechanism and settle this ambiguity, especially as experimental efforts are just emerging; the proper identification of fatigue is critical for the design and utilization of CNT-based structural materials/applications.

The strength limits of an ideal CNT and even the dependencies on its helicity and temperature are well understood in theory (*8*), supported also by experiment (*9*). In contrast, their assemblies into bundles or fibers remain much weaker (*10*–*12*). In this context, where the interfaces between nanotubes have frictional load transfer, the fatigue failure of CNT assemblies is very different from its constituents. Since their interfacial interactions are much weaker than their cohesive interactions, cyclic loading of CNT fibers and yarns (*13*) produces irreversible slips with each cycle. As a consequence, the time and length scales pertinent to individual CNTs and their assemblies may vastly differ, calling for a multiscale modeling approach. At the level of an individual CNT, atomistic simulations using density functional theory–based tight binding (DFTB) (*14*) and long-range bond-order potential (LCBOP) for carbon (*15*) to quantify the energetics of defects formation are combined with kinetic Monte Carlo (kMC) to bridge an inherent time scale gap. On the other hand, representing mesoscale CNT assemblies, such as bundles and ropes, mandates the bridging of a wide length-scale gap. Adopting an expedient coarse-grained CNT model (*10*) thus makes it possible to probe the mechanical behavior upon cycling load of micrometer-scale CNT bundles (see also section S1 for a figure panel schematic of the multiscale approach).

We show that individual pristine CNTs appear indefatigable under typical cyclic load, not accumulating internal structural damage; instead, probabilistic mechanical failure occurs via abrupt brittle fracture and therefore cannot be qualified as fatigue. On the contrary, in CNT bundles, a fatigue behavior, with definitive damage accumulation, is revealed and its mechanism is identified: a strain ratcheting, resulting from the interplay between slip and incomplete elastic recovery upon loading/unloading, leading to damage accumulation, not occurring under static load even of equal amplitude.

Department of Materials Science and Nanoengineering, Rice University, Houston, TX 77005, USA.
*Corresponding author. Email: biy@rice.edu

RESULTS

CNTs can follow two routes to mechanical failure (*8*, *16*, *17*): (i) a purely brittle one and (ii) a route with some plastic deformation before nanotube rupture. Both routes depend on various parameters, among which crucial are the strain, temperature, and the chiral angle. In brief, tensile strain reduces the thermal activation barriers for breaking the most strained bonds (closely aligned to the tube axis) and the barriers for rotation of the highly sheared bonds (aligned near perpendicular to the tube axis) (*8*). Therefore, zigzag and near-zigzag tubes have lower breaking strain for brittle failure, while armchair and near-armchair tubes rather fail by plastic yield. Under cyclic loading, if neither mechanism is activated during each cycle, the resulting failure may not be ascribed to fatigue, as is explored further below.

The brittle route to CNT failure

We consider first the pure brittle route using a pristine (10,0) nanotube as a representative. Under uniform axial strain ε, the shortest path to complete tube failure is when its bonds are broken in a way that the crack propagates along the circumference, in any cross section. The smallest possible initial crack for such a path is a single broken C—C bond along the tube axis, schematically shown in the bottom inset of Fig. 1A. To mimic thermal fluctuations in the strained lattice, the length of such a bond is gradually increased in increments of ≃0.1 to 0.2 Å, while the remaining lattice is relaxed, at a DFTB level (see Materials and Methods for details), which is similar to the procedure adopted in (*18*). This stepwise elongation is continued even as the neighboring bonds break and eventually leads to the cleavage of the tube into two disconnected fragments (Fig. 1A, top inset). The energy change due to this process can be used to estimate the thermal barrier for the crack initiation/propagation at different ε as shown in Fig. 1A. A piecewise, nearly linear relationship is apparent, where the transition point at $\varepsilon \simeq 13.5\%$ represents the breaking strain ε_b, as the activation barrier above ε_b is much smaller than $k_B T$. For $\varepsilon < \varepsilon_b$, a linear fit $E^*(\varepsilon) = E_0 - E_1\varepsilon$ gives $E_0 \equiv E^*(\varepsilon \to 0) \simeq 14.4$ eV. Although approximate, this estimate makes it clear that $E_0 \gg E^*(0.1) \simeq 3.7$ eV, and therefore, the time scales, viz. the rates of these processes, will differ by many orders of magnitude.

A crucial observation from the bond elongation plots (top inset in Fig. 1A) is that all the curves (at least for $\varepsilon < \varepsilon_b$) are monotonic and without any local minima, indicating an absence of metastable cracks or lattice trapped states (*16*–*18*). Some minor features such as small kinks appear whenever the neighboring bonds are presumably broken. This suggests that failure of a pristine tube can only be abrupt, brittle (i.e., no discernible nucleation or development), and below its breaking strain it simply takes time *t*. In this scenario, strain ε(*t*) is the sole parameter controlling the barrier for nanotube fracture, and the failure probability is cumulative

$$P(t) = 1 - \exp\left[-\int_0^t \Lambda(\tau)\, d\tau\right] \quad (1)$$

where $\Lambda(t) = \nu \exp\{-[E_0 - E_1\,\varepsilon(t)]/k_B T\}$, with $\nu \sim 10^{13}$ Hz; a barrier-strain linearity has long been empirically established and applied in the kinetic theory of the strength of solids (*19*, *20*) [some attempts to apply the same concept to time-dependent CNT fracture have used a quadratic strain dependence also, without a clear physical justification (*21*)]. In a state of fluctuating (or cyclic) strain, the maximum likelihood of failure occurs whenever the strain peaks. During tensile cyclic loading with a sine profile, $\varepsilon(t) = \varepsilon_0[1 + \cos(\omega t)]/2$ (Fig. 1B, inset), the integrand $\Lambda(t)$ decays rapidly away from the peaks, where $\varepsilon/\varepsilon_0 \simeq 1 - (\omega t)^2/4$. Over one cycle, denoting $\lambda = \int_0^{2\pi/\omega} \Lambda(t)\, dt$, the failure probability of a tube simplifies to $1 - \exp(-\lambda) \simeq \lambda$, for $\lambda \ll 1$. Therefore, the survival probability over *n* cycles is $(1 - \lambda)^n \simeq 1 - n\lambda$. The number of cycles until failure can then be estimated from $n\lambda \sim 1$, by saddle-point integration of $\Lambda(t)$, which gives

$$n(\varepsilon_0; T) = (\omega/2\nu)\,(E_1/\pi k_B T)^{1/2}\,\varepsilon_0^{1/2} \exp\left[(E_0 - E_1\varepsilon_0)/k_B T\right] \quad (2)$$

plotted in Fig. 1B. The relation is formally akin to "strain-life" curves that characterize the fatigue life of a typical material (*1*). Notably, at low strain amplitude up to ≃5%, a pristine CNT has practically infinite life ($n \gg 10^{20}$) and, in this sense, behaves more like a macromolecule (rather than a material), exhibiting no fatigue

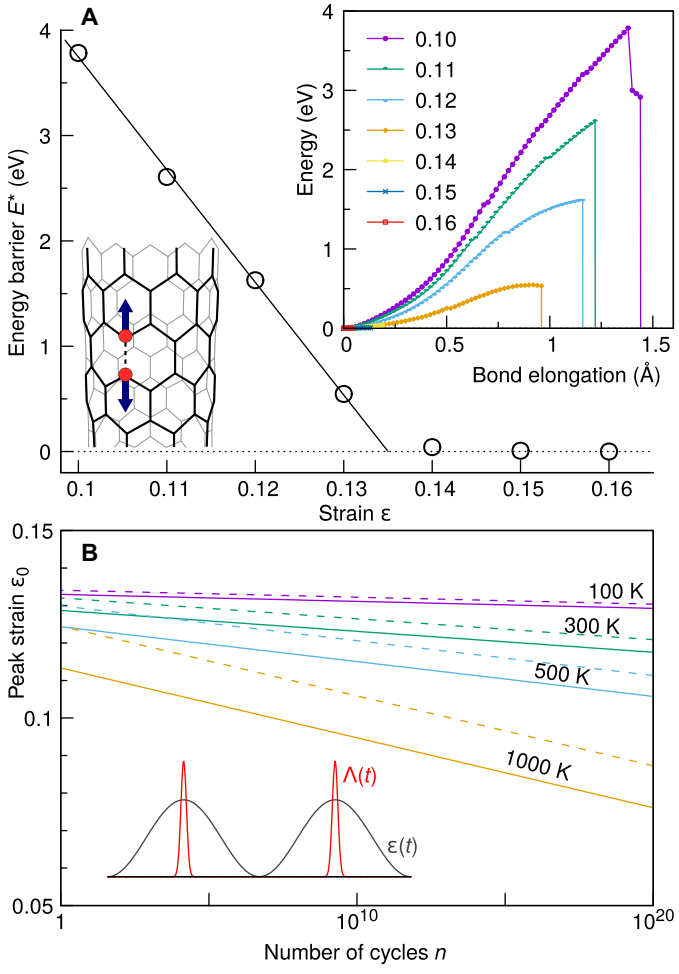

Fig. 1. Brittle failure of a CNT. (**A**) Bond-breaking barrier E^* for a (10,0) CNT computed using DFTB. Each data point is determined from the maxima of the energy versus bond elongation curves shown in the inset, calculated for a tube under tensile strain in the range of 10 to 16%. The line is a linear fit to the data for $\varepsilon \leqslant 13\%$, $E^*(\varepsilon) \simeq 14.4 - 106.9\varepsilon$ (eV). (**B**) Logarithmic-scale plot of the strain amplitude ε_0 versus number of cycles *n* until failure obtained from Eq. 2 for $T = 100$ to 1000 K at two different frequencies, $\omega = 1$ Hz (solid lines) and 1 MHz (dashed lines). The inset illustrates the ε(*t*) (gray) and failure rate (red) profiles over the time span of two cycles.

under cyclic tensile loading. Under this brittle route, with no pre-existing or nucleated defects and the inability to sustain stable cracks, no plastic strain is accumulated, and the nanotube after, say $\simeq 10^{20}$ cycles, is no different from a pristine "brand new" nanotube. This behavior reflects the stochastic nature of a CNT's brittle failure, rather than representing its fatigue life.

Mechanism of plastic deformation in a CNT

The other alternative route to CNT failure involves plastic deformation by incorporation of dislocation dipoles (*22*), as typically observed in low cycle fatigue of metals (*1*, *6*). Such a possibility arises when a Stone-Wales (SW) defect spontaneously nucleates by rotation of a C—C bond, resulting in a coupled pentagon-heptagon dislocation dipole 5|7/7|5. The SW defect also happens to be the prime point defect that can form in the pristine sp^2-carbon lattice, with energy lower than any other—vacancies, interstitials, or a pair of single dislocations (*23*). These defects are chirality preserving, viz. not disrupting the CNT lattice, unlike a single isolated dislocation; as a result, their presence may be virtually undetectable, at least by standard spectroscopies, which detect a chirality change or appreciable defect density.

The investigation of the plastic route to failure is performed using a (6,6) tube, without loss of generality, and stress-controlled load (see Materials and Methods). Figure 2 summarizes the results from DFTB calculations for an initially pristine tube of $L \simeq 5.2$ nm (with periodic boundary conditions applied axially to avoid edge effects) and depicts the enthalpy changes and enthalpy barriers of a sequence of bond rotations, which eventually form the shear band of the CNT (akin to persistent slip bands in metals) (*24*, *25*). An initially pristine armchair CNT has two families of identical bonds: perpendicular and slanted (±30°) to the tube axis. During axial loading, the former are under the highest shear and therefore have a lower barrier to rotate than the slanted bonds. This preference is observed for all $\varepsilon_0 > 0$ and leads to the first SW defect as shown in Fig. 2A (second image on the top). The energy and enthalpy barriers, $E^{\ddagger}$ and $H^{\ddagger}$, respectively, for these transformations are evaluated using the nudged elastic band (NEB) method together with Bell-Evans-Polanyi (BEP) principle (Fig 2A, inset), as explained in Materials and Methods.

Evidently, the first SW defect always lowers the CNT symmetry and (partially) lifts the degeneracy in bond rotation barriers for the two bond families, thereby localizing the activation site for the subsequent bond rotations to its immediate vicinity. To explore subsequent transformations, rotation barriers for all bonds in the tube need to be evaluated individually. These extensive calculations of strain-dependent $E^{\ddagger}$ from the second to the fifth bond rotations revealed that the kinetically most favored pathway for nonzero strain is along the shear band of the nanotube, as shown in the top images of Fig. 2A (for details, see section S2). At $\varepsilon_0 = 0$, the formation enthalpy ΔH monotonically increases with each bond rotation (at least up to the fifth bond) and is not the preferred pathway, even as the barriers decrease slightly. However, for $\varepsilon_0 \gtrsim 0.05$, the shear band pathway becomes more favorable in both energy and kinetics. At $\varepsilon_0 = 0.14$, the DFTB results show that the configurations from the second SW defect onward are unstable, and therefore, a tube should break as soon as the first SW defect has formed.

Although the shear band formation is the preferred kinetic pathway, other competing pathways do exist at every bond rotation, especially when the applied strain is reduced. This is shown in Fig. 2B for the second bond rotation at two strain values. Here, the two-SW shear band has lower energy and barrier, among other possibilities with slightly different bond rotations where the two 5|7 dislocations split apart or incorporate an octagonal ring (for brevity, we will refer to the three configurations as "sheared," "split," and

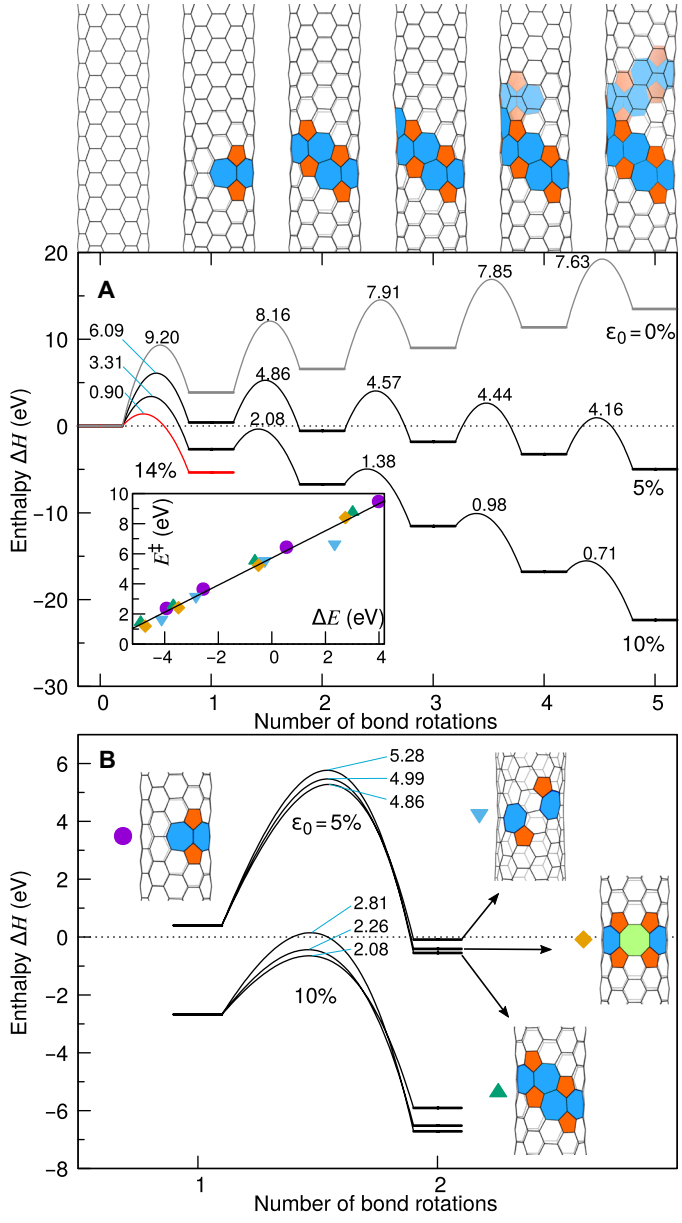

Fig. 2. Energetics and kinetics of CNT plastic failure. (**A**) Diagram of enthalpy change ΔH (horizontal bars, relative to a pristine CNT) for sequential bond rotations forming a shear band (top images, with 5|7 highlighted) at different tensile strains in the range of $\varepsilon = 0$ to 0.14. The inset shows the relation between the DFTB-computed bond rotation barriers $E^{\ddagger}$ and energy differences ΔE for final configurations as indicated in (B) with the corresponding symbols; the line is a linear regression to the computed points, $E^{\ddagger} \simeq 5.7$ eV + 0.9ΔE. The energy barriers $E^{\ddagger}$ obtained from this expression are indicated (in electron volts) for all transitions (shown schematically as thin parabolic segments). (**B**) Comparison of other possible configurations after two bond rotations, close in energy to a shear band: SW-defect splitting (5|7⋯7|5) and defects configuration including an octagon (5|7/5|8|5/5|7) (*22*).

"octagonal," respectively). Considering the multiplicity of these configurations (viz. 4 for sheared, 4 for split, and 2 for octagonal), the relative probabilities of these paths can be evaluated, e.g., at 1000 K. At $\varepsilon_0 = 0.05$, the sheared:octagonal:split configurations are 81.4:18.0:0.6% probable, whereas at $\varepsilon_0 = 0.1$, the relative probabilities are 88.9:11:0.02%, respectively.

The results in Fig. 2 highlight the early steps a pristine nanotube undergoes toward plastic deformation, which essentially sets its overall time scale. An expedient way to propagate the CNT in time along the plastic route and capture failure is to use (on-the-fly) kMC (*26*, *27*) using the LCBOP potential (*15*). kMC has been instrumental in bridging the time scale gap in other problems involving CNTs, from catalytic growth (*28*) to electron irradiation (*29*). Ideally, the kMC simulations should include all possible processes such as bond rotations and bond breaking. However, as discussed earlier, single-bond cracks were never found to be stable at low strain levels, and barriers to break several bonds simultaneously, which may be necessary to form a stable crack, are exorbitant. Therefore, only bond rotations are considered as feasible processes in the kMC simulations.

Figure 3 summarizes the results of the kMC simulations (see Materials and Methods) for different initial strain levels, comprising a total of more than 100 trajectories. A sample kMC trajectory for each of the ε_0 values in the range 6 to 14% is shown in Fig. 3 (A to E). Animations of these trajectories are also provided in movie S1. As expected from the DFTB results (Fig. 2), the kMC trajectories show preference to the formation of the shear band in the first few steps in most cases ($\varepsilon_0 = 10$ to 14%). However, for $\varepsilon_0 \lesssim 8\%$, the splitting of the first SW was found to be kinetically favored. This is perhaps an undesirable consequence of the LCBOP potential, where further investigation revealed that the energetic preferences at lower strain are in a different order than DFTB results. Generally, the formation energies of various SW defect configurations in LCBOP are found to be underestimated by up to a few electron volts compared to DFTB, an uncertainty known even for different flavors of DFT (*30*) (an expedient correction scheme is outlined in Materials and Methods and section S3). Nonetheless, the two defect configurations (Fig. 2B) are very closely related, and the SW splitting (5|7⋯7|5) simply presents a different pathway of nonvanishing probability. A more general observation from Fig. 3 (A to E) is the ductile to brittle transition as strain is increased, where lower ε_0 results in larger plastic strain (at $\varepsilon_0 = 6\%$, Fig. 3A, the tube may not break for the entire duration of the simulation), while at higher strain, e.g., $\varepsilon_0 = 14\%$, the tube fails after two to three bond rotations. The plastic strain in the final geometry (after 100 bond rotations) in Fig. 3A is 43% due to substantial necking, with (6,6)→(5,0) chirality change, viz. twofold reduced diameter, commonly associated with CNT "superplasticity" (*22*, *31*).

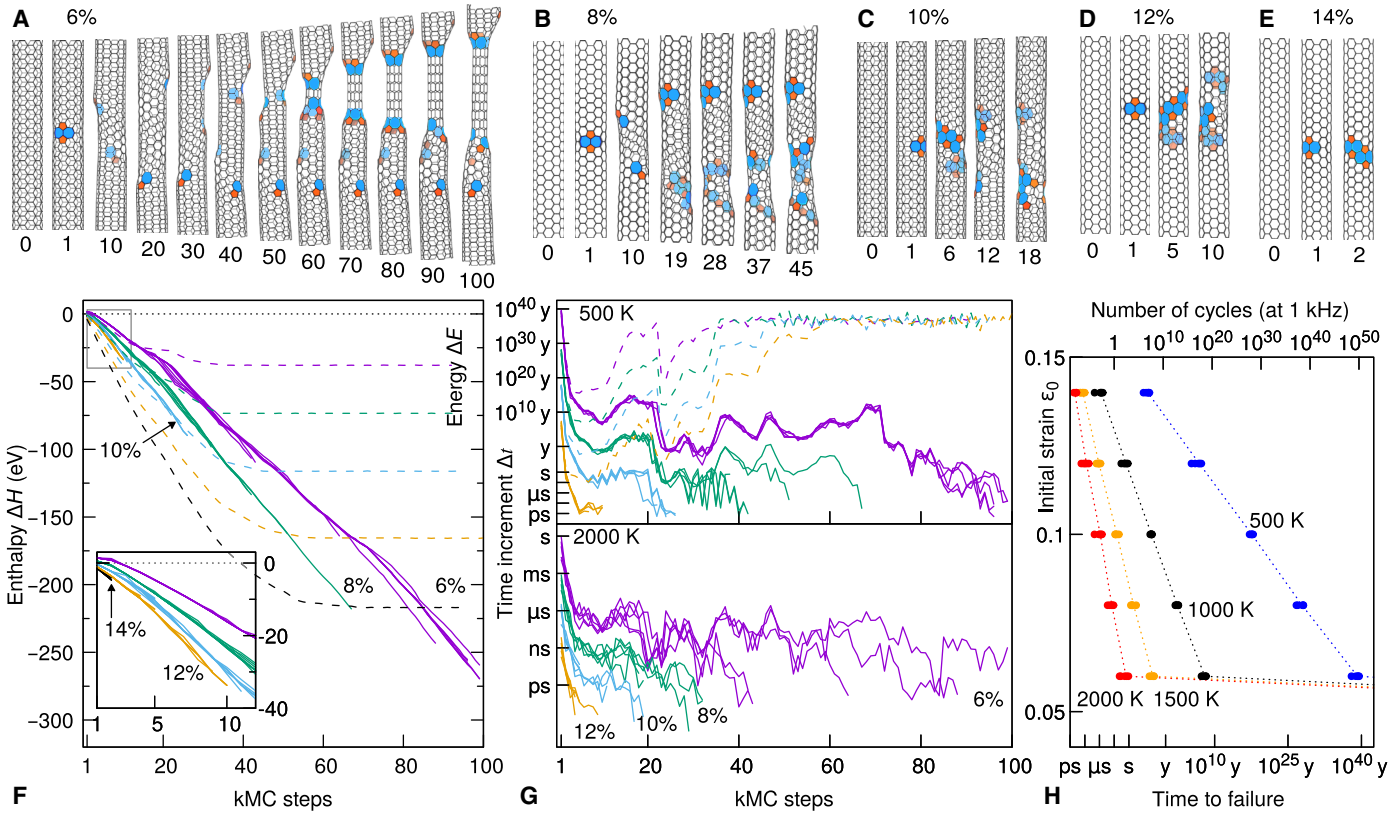

Fig. 3. kMC trajectories of CNT plasticity. (**A** to **E**) Representative CNT geometry evolution from kMC trajectories for initial strains in the range of 6 to 14% at 1000 K. The number of bond rotations (viz. number of kMC steps) is indicated under the individual images. (**F**) Enthalpy change ΔH due to bond rotations along the kMC trajectories for stress-controlled loading at different values of initial strain ε_0 (full lines, left axis). The inset is a zoom-in view of the gray-framed area above. Dashed lines (right axis) correspond to strain-controlled loading. Both stress-controlled and strain-controlled trajectories are shown as animations in movie S1. (**G**) Time increment Δt for kMC trajectories at different strains for two temperatures. (**H**) Strain-life curves at different temperatures.

All kMC trajectories for a given ε_0 with random initialization display very similar quantitative trends even as T is varied, as demonstrated by the nearly identical ΔH evolution (overlapping curves) in Fig. 3F. The solid curves, for the stress-controlled loading, show that after the first few bond rotations, the enthalpy decreases almost linearly. This decrease may not be intuitively obvious especially since $\Delta E > 0$, because creation of more defects is energetically costly, while simultaneously there is no strain relief due to the application of a constant stress (σ_0) on the boundaries of the simulation cell. The decrease stems from the second term (boundary work) in $\Delta H = \Delta E - \sigma_0 \Delta V$, whose magnitude ($\Delta V \sim \varepsilon$) is much larger than the change in energy ($\Delta E \sim \varepsilon^2$).

For additional context, the dashed curves in Fig. 3F are the results for strain-controlled loading, where the tube length is kept fixed after elongation to the initial strain ε_0 at the beginning of the simulation. It is seen that at least for the first few bond rotations the ΔE energy trend closely resembles that for ΔH in the stress-controlled loading. However, ΔE soon saturates to a stationary value, whereupon no previously unidentified configurations are created, and the system oscillates between a few select configurations. This is demonstrated in movie S1. The ΔE saturation can be explained by the ability of plastic deformation to mitigate the initial elastic strain in the tube. From Fig. 2, the bond rotation barriers $E^{\ddagger}$ are expected to be much larger when the tube strain is low. Thus, with each kMC step, the strain in the tube decreases, slowing down the kinetics of new bond rotations, and eventually the system behaves almost like an unstrained tube.

The key differences in the kinetics of these trajectories can be seen in Fig. 3G, where the time increments Δt for each kMC step are plotted for $T = 500$ and 2000 K. As can be expected, higher T significantly accelerates the plastic deformation, reducing the time scale from astronomical to 10^{-9} to 1 s. Even then, one invariant observation across all temperatures is that the nucleation of the first SW defect is always the slowest (by several orders of magnitude) and pivots the entire time scale of failure through the plastic route. This suggests that starting from a pristine CNT, the longest mean waiting time, $\langle \Delta t \rangle = 1/R$, with R the (total) cumulative rate, is almost entirely for the formation of the first SW defect, and all subsequent steps are much faster. For illustration, Δt values along strain-controlled trajectories are also shown (dashed lines for $T = 500$ K; Fig. 3G), revealing that the time scale of plastic deformation initially follows the stress-controlled behavior but subsequently deviates and becomes comparable to that for the first SW defect. This demonstrates that as soon as the plastic strain mitigates the elastic strain, there is a lack of a driving force to cause any further plastic deformation.

Notably, for stress-controlled loading, Δt is nonmonotonous, with a number of characteristic "bumps" (substantial slowdowns), which occur whenever a new SW defect is nucleated instead of further propagation of an existing defect. This is possibly because further propagation at those stages has a similar barrier as a new SW nucleation, away from the activation site. However, because of the local stress enhancement (due to stress concentration) caused by the existing defects that reduce $E^{\ddagger}$, such a process occurs markedly faster than in a pristine tube.

A complete summary of all kMC results in the form of strain-life curves for the plastic route is shown in Fig. 3F, obtained by integration of all time increments giving the total time to failure. At 500 K, a CNT will survive from a few hours at $\varepsilon_0 = 0.14$, to indefinitely at $\varepsilon_0 = 0.06$, while at 2000 K, it will fail within $\lesssim$1 s for any strain above 0.04. At $\varepsilon_0 \lesssim 0.04$, for all temperatures, the CNT behaves as a two-state system, oscillating between the initial pristine state and the tube with one SW defect. This is because, at these low strain levels, after the nucleation of the first SW, which in itself is very improbable, the next favored step is to always heal the SW back to the pristine configuration. This then suggests that 4% strain is a limit, akin to the endurance limit of the nanotube, where the tube has a truly infinite life.

From Fig. 3, it is clear that at ambient conditions, not too high T, an individual CNT is indefatigable, i.e., it does not undergo fatigue failure especially because of the huge disparity between the relevant time scales of defect kinetics Δt and any kind of cyclic loading with frequency ω, because it can always be shown that $1/\omega \ll \Delta t$. However, if a nanotube is already defective, fatigue may occur on a more practical time scale. This is, in fact, suggested by the strain-controlled loading simulations, where the defect accumulation stops after tube strain is mitigated. If this specimen is removed and used later in another strain-controlled loading, it will have a memory of its prior "experience," and subsequent defects and their time scales will depend on its prehistory. Further discussion about the strain-life curves for already defective tubes are also provided in section S4.

Fatigue in "bulk" CNT assemblies

The indefatigability of nanotubes is only relevant if they are defect-free and ultralong (centimeter to meter range), to be directly tested or used in structural applications, either individually, as in CNT coils (*32*), or in the form of macrobundles where each tube spans the entire length, as in (*3*). However, practice (*10*–*12*) often prevents these realizations, and instead, the tubes are shorter and much thinner than the bundle comprising them, typically with 10^4 to 10^5 of similar hexagonal close-packed CNTs over cross section. For simplicity, one assumes that they all have the same length L and diameter d and are arranged in a 3D face-centered cubic (fcc)–like lattice (*10*, *33*). This constitutes a finite yet representative volume element that can be used to characterize the bulk behavior of a CNT bundle. In a bundle, a crucial aspect is, of course, the load transfer at the interfaces of adjacent CNTs, characterized by the interface frictional force per unit length, f (*10*). The intertube friction can be a bottleneck to the strength of the entire bundle, allowing its elements to slip under any load above ~fL, commonly well below $s_i d^2$, with s_i being the tube's intrinsic strength. However, whether this dissipative interface itself could cause fatigue in CNT bundles is nonobvious and is important to explore.

In the stress-controlled cyclic loading (Fig. 4A), the stress is ramped up to nearly full tensile strength s of the bulk bundle element, to stress amplitude $\sigma_0 = 0.98s$. The results differ notably from a single tube because during unloading a slightly different path is followed, and plastic (permanent) strain is accumulated after each cycle. The choice of this high σ_0 allows us to track a complete life cycle of this system, which in this particular case is $n = 46$, after which the bundle fails because of complete slippage of some of the tubes in the cross section of the bulk bundle. The failure due to this type of loading is further explored in Fig. 4C, where the mean gap length $\langle \delta \rangle$ between axial neighbors [along the same thread, cf. (*10*)] is plotted as a function of the simulation time. The saw-tooth shape of the curve is due to the cyclic expansion-contraction of the gaps, synchronous with load cycle, because the tubes adjacent to the gap experience local stress enhancement causing a higher strain amplitude than anywhere else in the bundle. The amplitude of the

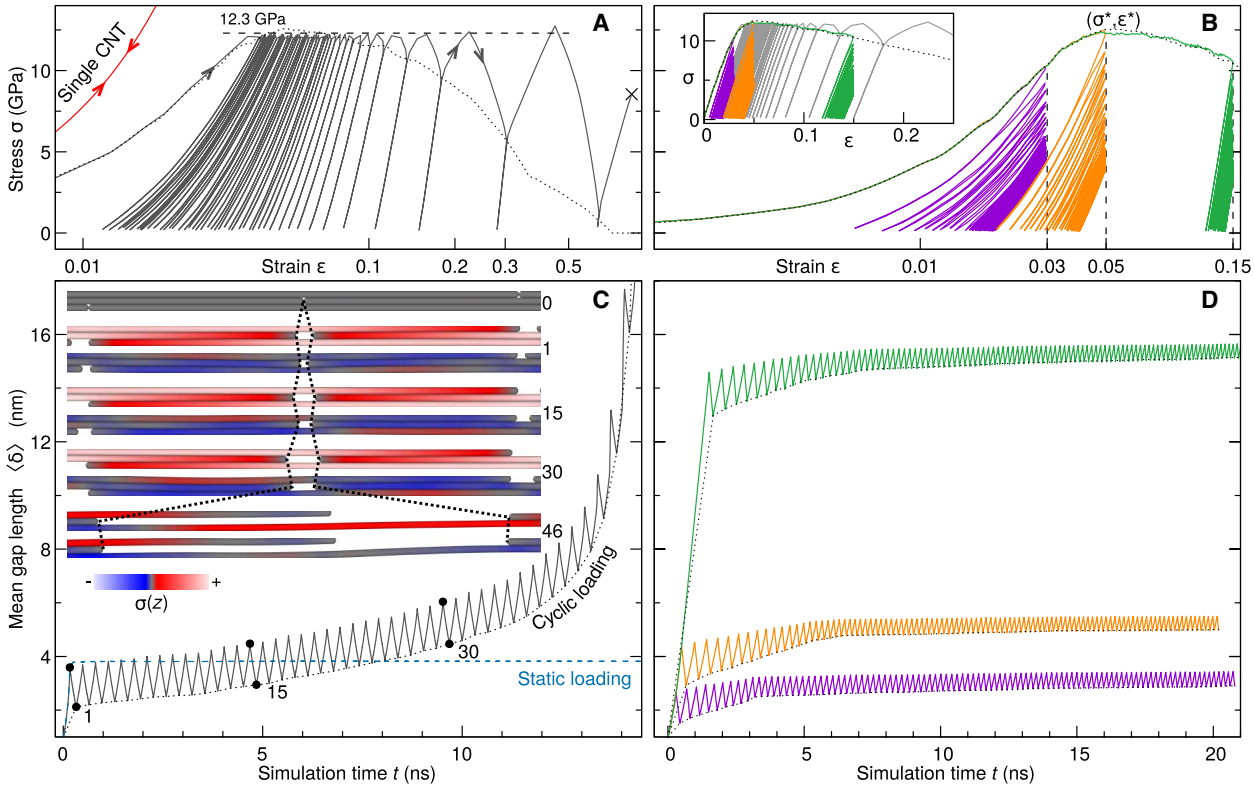

Fig. 4. Fatigue of bulk CNT assemblies. (**A** and **B**) Representative σ-ε curve (full line) for a bulk bundle element of length $L = 100$ nm and friction $f = 0.01$ nN/Å subject to cyclic loading: (A) stress control with a constant amplitude $\sigma_0 = 0.98s$ (dashed line) and (B) strain control with constant strain amplitudes of $\varepsilon_0 = 0.03$, 0.05, and 0.15. For comparison, the monotonic loading of the same system is given as a dotted line in both (A) and (B), with the maximum indicating the strength of the bulk bundle s from (*10*), and the labeled red line in (A) shows the hysteresis-free σ-ε curve for an individual CNT. Note the logarithmic scale of the ε-axis. The × mark indicates the bundle failure, occurring after $n = 46$ cycles in (A). The inset in (B) shows the σ-ε curves for both loading conditions with linear ε-axis for comparison. (**C**) Mean gap length ⟨δ⟩ versus simulation time t for a bulk bundle element corresponding to (A). The dotted line connects the valleys of each cycle to indicate the permanent changes in ⟨δ⟩. The inset shows the simulation snapshots (with color-coded stress distribution) of the initial configuration ($t = 0$) and subsequent changes in gap length after the cycles as labeled on the right, for both the peak and the valley of the cycle. These points are also marked by black dots on the ⟨δ⟩ curve. For reference, the blue dashed curve shows ⟨δ⟩ of a statically loaded bulk bundle element. (**D**) The same as in (C), but for the case of strain-controlled loading in (B).

saw-tooth curve is thus directly controlled by the stress level in the tube and the stiffness of the nanotubes. The lower envelope tracks the permanent cumulative change in ⟨δ⟩, which initially increases almost linearly, but then grows exponentially, until failing after the 46th cycle.

Figure 4C and movie S2 also showcase that if the same bulk bundle element is subjected to static loading for the same duration, ⟨δ⟩ and ε saturate after reaching the maximum applied load σ_0. This is perhaps nonobvious and even counterintuitive, since cyclic load when time-averaged is half of the static load in this case, and yet leads to failure of the bulk bundle element much earlier. The reason for this different behavior is due to the interplay of slips at the extension phase, and an incomplete recovery caused by elastic force push-back at the load-release phase, a particular ratchet-up mechanism that operates and results in gradual damage accumulation (in the form of increasing gaps between the CNTs) and eventual failure after large number of cycles.

In the case of strain-controlled loading (Fig. 4B), three instances of strain amplitude are demonstrated, ε_0 = 0.03, 0.05, and 0.15. In each case, during the loading phase of the cycle, the box is elongated to match the prescribed strain value, while during the unloading phase, the stress is relaxed back to zero. As a result, the initial length of the bundle changes with each cycle since whatever plastic strain accumulates during the loading phase becomes permanent, and therefore, the remaining end-to-end displacement diminishes with each cycle, asymptotically approaching zero. This is further demonstrated in the corresponding plots for ⟨δ⟩, where the amplitude of the saw-tooth curves reduces as the cycles progress, indicating a reduction in the overall stress level. Here, the three strain values demonstrate that this fatigue behavior shows no significant difference whether the strain amplitude lies below, at, or above the critical strain ε* (strain at maximum stress σ*; cf. Fig. 4B), which also marks the transition from an elastic interface to a plastic interface (*10*). Note that for the stress-controlled loading, the interface is always elastic, as this transition point ε* can never be crossed.

Fatigue of CNT bundles

The fatigue of a bulk bundle serves as a guideline for the more practical realization of the bundles where the width is finite, and the lengths of the nanotubes are normally distributed. The same protocol as in the preceding section is applied for a bundle of finite diameter (see the inset image in Fig. 5D). Although reaching the fatigue life of

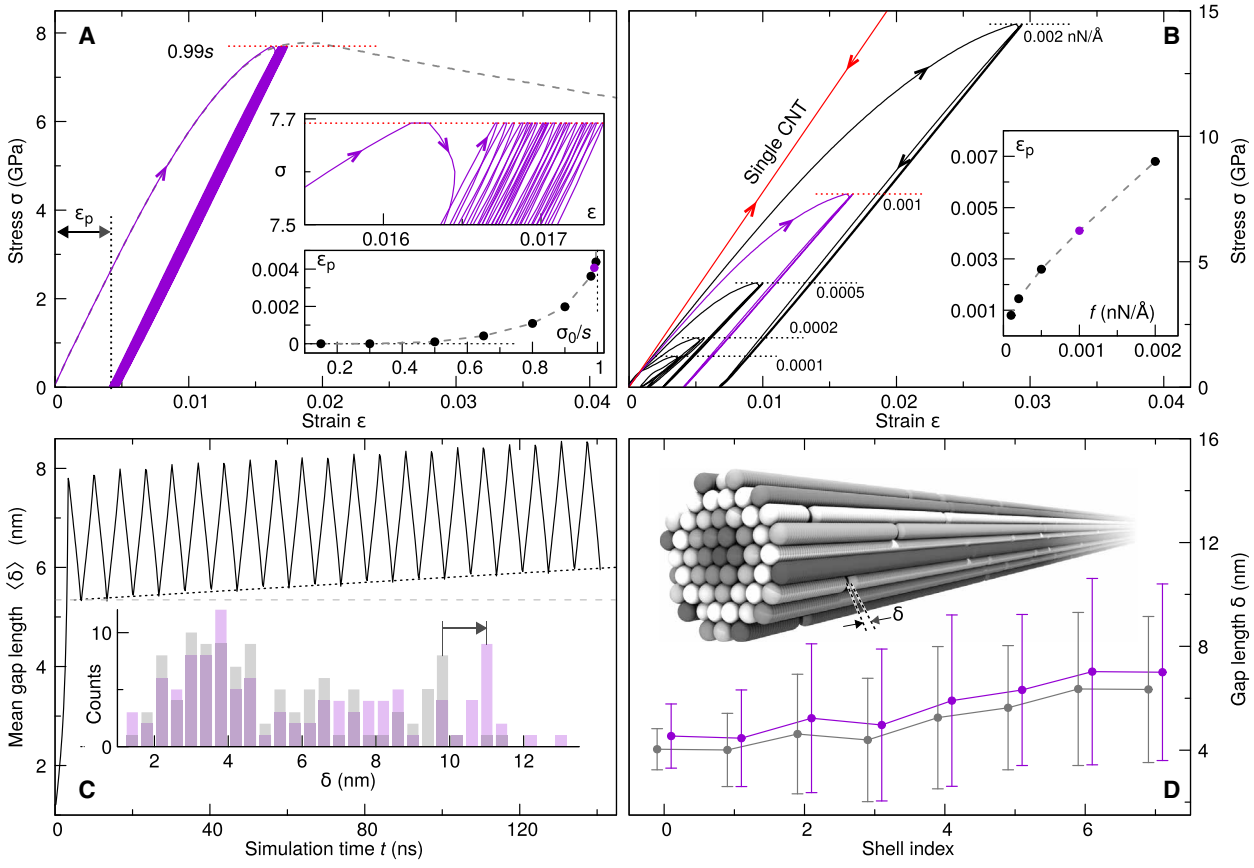

Fig. 5. Cyclic loading of a CNT bundle. (**A**) Representative σ-ε curve for a CNT bundle of variable-length CNTs with mean length $\langle L \rangle = 1$ μm and friction $f = 0.001$ nN/Å. The dashed line shows the monotonic loading of the same system (*10*). The top inset shows a zoom-in view of the plot around the stress amplitude of $\sigma_0 = 0.99s$. The bottom inset shows the permanent strain after the first cycle ε_p versus σ_0/s (dotted lines mark the limits $\varepsilon_p = 0$ and $\sigma_0/s = 1$). (**B**) Stress-strain curves for a few cycles to capture ε_p as f is varied. Dotted lines correspond to $0.99s$, where s is the strength determined from the corresponding monotonic curves for the same product fL as in (*10*). The red solid line shows the hysteresis-free σ-ε curve for an individual CNT. Inset shows the relationship between ε_p and f. (**C**) Mean gap length $\langle \delta \rangle$ as a function of simulation time. The dotted line is a linear fit to the δ values at the end of each cycle, and the horizontal dashed line marks the $\langle \delta \rangle$ value after the first cycle. The inset shows a histogram of δ for all 110 gaps after the first (gray) and last (violet) cycles. (**D**) Average gap length (dots) and its variation (error bars) due to the proximity to the periphery; color coding is the same as in (C). The inset illustrates the shell indexing.

such a realistic-size bundle is hardly computationally feasible, even in a coarse-grained simulation, characteristic behavior is revealed already in the first few cycles, as illustrated in Fig. 5A, where we have been able to realize 21 cycles at maximum load approaching the bundle strength, $\sigma_0/s = 0.99$. Notably, a large permanent strain, $\varepsilon_p = 0.4\%$, is accumulated already in the first cycle. In the subsequent 20 cycles, plastic strain ratchets up at a nearly constant rate of ≃0.005% per cycle. This process can be seen in the top inset in Fig. 5A, where the maxima of the stress curve are incrementally offset in strain. However, in practical applications design, load amplitudes σ_0 are prescribed to be well below the ultimate tensile strength s. Tests of the ε_p dependence on σ_0 (Fig. 5A, bottom inset) show that ε_p is vanishing for any $\sigma_0/s \lesssim 0.5$, and no residual strain could be detected even after 10 cycles for $\sigma_0/s \leqslant 0.3$. This also suggests that the endurance limit of this bundle can be ~0.3 to 0.5s, in surprising accord with the rule of thumb for most steels and copper alloys (*1*). Even so, the endurance limit of these metal alloys (0.2 to 0.5 GPa) is far lower than the bundle (2.3 to 3.5 GPa) in Fig. 5A.

The burst-like behavior of ε_p is due to the incomplete elastic recovery of the nanotubes as the load is released, which leads to some parts of the tubes being stretched and even compressed as found for the bulk bundle element in Fig. 4C (inset). This has also been experimentally observed for graphene interfaces (*5*) and is common in various bulk (3D) materials [associated with strain ratcheting (*34*, *35*)]. Because we consider a single finite-width bundle (fixed geometry parameters and maximum loading level), ε_p is expected to depend also on the tube-tube interface shear properties, characterized by the interface friction f. This is demonstrated in Fig. 5B where two cycles are realized for a range of $f = 0.0001$ to 0.002 nN/Å, with the respective residual strain after the first cycle ε_p plotted in the inset. Overall, for the larger f values, scaling is essentially linear, $\varepsilon_p \sim f$, while for vanishing but finite friction, ε_p falls off slightly faster. This can be attributed to decreasing slope/stiffness upon unloading, reflecting the ease of restoring interface contact when friction is reduced, aided by the ubiquitous capillary action.

Figure 5C further reveals a very similar trend in $\langle \delta \rangle$ as in the bulk case for the stress-controlled loading, namely, the initial almost linear increase with the number of cycles. However, with distributed nanotube lengths and their specific spatial arrangement, all the gaps, initially of the same length, undergo different levels of increments

due to very different stress concentrations. This is demonstrated in the inset of Fig. 5C, showing the histogram of δ after the first and last cycle. Some noticeable shifts of peaks are observed especially for the larger gaps (as marked by the arrow).

The distribution in gap lengths led us to a deeper exploration into the role of the peripheral/surface gaps (*10*), which should experience an overall heightened stress concentration effect due to reduced number of neighbors. The plot in Fig. 5D shows ⟨δ⟩ after the first and last cycle as a function of the shell index (gray levels in the inset), which defines equidistant sets of tubes from the bundle axis. The plot demonstrates that, in general, gaps become larger as the shell index increases, with peripheral gaps being the largest, after both the first and last cycles.

DISCUSSION

In light of our findings related to individual nanotubes, the recent experimental observations that "fatigue failure … is global and catastrophic without progressive damage" (*3*, *4*) are difficult to reconcile with actual fatigue in pristine nanotubes and graphene under ambient conditions. The cyclic loading tests in (*3*) (via acoustic resonance) found a CNT to be "super-durable," exhibiting excellent fatigue resistance. CNT failure, attributed to fatigue, is observed after ~10^3 to 10^7 cycles depending on the magnitude of the applied load, implying longitudinal strain that can be locally as high as ≃15%. This is admittedly an upper estimate based on specific simplifying assumptions (*3*) (e.g., lack of longitudinal displacement, resulting in zero strain at the point of maximum deflection and maximum strain at the supported CNT ends). More realistic constant tension model and discrete elastic rod simulations (*36*) result in maximum strain ~5%, where we show that a pristine CNT is indefatigable. However, as it can be deduced from Fig. 3, preexisting defects (i.e., starting from an already defective tube; see section S4) can easily result in a gradual reduction in strength on minute or hour time scale. The reportedly strong friction between the suspended CNT ends and the substrate can be associated eventually with covalent bonding, which presumably introduces sp^3-"defects" in the pristine sp^2-carbon lattice of the CNT wall (*10*). In addition, the interfaces between the decorating TiO_2 nanoparticles, used in the experiment (*3*), and the CNT might be prone to covalent cross-linking (*37*). However, these possibilities may be difficult to corroborate in experiments.

In summary, by using atomistic computations in conjunction with kMC simulations, we establish a rigorous quantitative ground for CNT behavior: Individual pristine nanotubes, essentially macromolecules of sp^2-C, do not undergo fatigue under ambient temperatures (as high as 500 K) for a wide range of loading frequencies [experimentally, ~500 Hz (*3*)]. This is because the time scale of defect formation in a pristine nanotube is always far greater than the time period of any mechanistically realizable cyclic process, with the bottleneck being the nucleation of the first SW defect. Exploring both brittle and plastic failure routes demonstrates that "defect free" nanotubes only experience brittle, abrupt failure. The tensile nature of loading used here is elementary, which can be further applied to more complicated situations when nanotubes may undergo bending or buckling, and thus, the localized tensile stresses instead play a role in defect kinetics. Even under these conditions, the local strain should never reach the high levels ($\varepsilon_0 \gtrsim 14\%$) necessary for spontaneous nucleation of SW defects (*38*). Graphene shares the same carbon honeycomb lattice and SW-defect energetics; thus, pristine graphene should be indefatigable as well (the presence of edge, however, will possibly play a role).

On the other hand, when assemblies of nanotubes undergo cyclic loading [experimentally, frequencies used so far are ~0.1 Hz (*13*, *39*)], their interfaces, much weaker compared to intrinsic CNT strength, can register a permanent/residual slip during each cycle, which is a characteristic feature of fatigue failure [interfacial slip is operable also in multilayer graphene assemblies as revealed in both experiment and coarse-grained simulations (*40*, *41*)]. Despite this, the endurance limit of these assemblies can be as high as ~30 to 50% of their strength, which for state-of-the-art nanotube fibers [with $s \simeq 10$ GPa (*42*)] could provide significant fatigue resistance, much higher than other commonly used structural materials, and for all conceivable working conditions. Thus, the present multiscale approach offers a new insight into a fundamental phenomenon, helping to interpret or predict nano- and mesoscale mechanical response of CNT assemblies upon cyclic loading.

MATERIALS AND METHODS

DFTB calculations

DFTB calculations (Figs. 1 and 2) are performed with the DFTB+ code (*43*), using the matsci-0-3 Slater-Koster parameter set for C. All bond-rotation barriers (Fig. 2A, inset) are determined by using the climbing-image NEB method (*44*) in the Atomic Simulation Environment (*45*) using seven images.

Stress-controlled loading

This mode is essential because in strain-controlled loading the tube length is kept fixed, and during the course of plastic deformation, the accumulated plastic strain will eventually be large enough to subdue the overall (far-field) elastic strain significantly. As a consequence, since volume is not conserved, pressure, energies, and energy barriers should be replaced with enthalpy and enthalpy barriers [see section S2 and also discussion in (*46*)]. In this setup, the physically relevant quantity is deemed to be the strain of the pristine tube, as the numerical value of stress in a tube depends on its diameter. The stress-controlled loading is realized by first elongating the pristine tube (viz. the simulation box) according to a chosen strain ε_0 and maintaining the corresponding axial stress, $\sigma_z(\varepsilon_0) \equiv \sigma_0 = \text{const}$, during the simulation. The value of σ_0 is then referred to by the initial strain value ε_0, signifying the strain that was applied to the initial defect-free, pristine tube.

Estimation of energy and enthalpy barriers

The SW bond rotation occurs on a time scale of ~0.1 ps (*17*), which is much faster than the typical speed of mechanical relaxation for the entire tube ~L/c, where L is the length of the tube and $c \sim 10^4$ m/s is the speed of sound in the CNT. L/c represents the characteristic time needed to undergo mechanical relaxation in response to the applied (far-field) stress σ_0 as soon as bond rotation occurs. Thus, the bond rotation (rapid degree of freedom) can be treated as an instantaneous process, which thus occurs at a constant volume (CNT length, slow degree of freedom) condition instead of constant pressure (stress), and therefore, the energy change ΔE and $E^{\ddagger}$ are computed at constant tube length. One can invoke here a remote analogy with the Born-Oppenheimer approximation, where the electronic (fast) dynamics can be determined at fixed nuclear

coordinates (slow degrees of freedom). Once a bond rotation is executed, the tube is relaxed to equilibrate the stress back to σ_0, and the corresponding enthalpy change ΔH (and enthalpy barrier $H^{\ddagger}$) is obtained by adding $-A\sigma_0\Delta l$ to ΔE (and $E^{\ddagger}$), where A is the cross-sectional area and Δl is the change in length due to relaxation. Since the calculation of the barriers for all possible bond rotations is computationally intensive, we use the BEP principle to estimate them directly from ΔE. This simplification is well justified and can be generalized to all bond rotations here, as shown in the inset of Fig. 2A, where NEB barriers for three other bond rotations were also evaluated, showing fairly good linear correlation, $E^{\ddagger} \propto \Delta E$. It is noteworthy that the linear relationship holds for $|\Delta E| \lesssim 4$ eV, which possibly encompasses all possible bond rotations considered here for all tensile strains. In addition, ΔE and $E^{\ddagger}$ are found to depend linearly on tensile strain (*8*), i.e., corresponding rates (viz. time scale) will have exponential strain dependence spanning multiple orders of magnitude.

kMC simulations

kMC simulations (Fig. 3) are performed in LAMMPS (*47*) with the LCBOP potential (*15*), using a rejection-free scheme (*26*, *27*). A kMC step includes evaluation of rates, $r_i = \nu \exp(-E^{\ddagger}_i / k_B T)$, for all possible bond rotations (performed at constant volume to obtain ΔE_i for the ith bond, from which the barrier $E^{\ddagger}_i$ is estimated using the BEP principle), selection and execution of a single bond rotation, and incrementing the simulation clock by $\Delta t = -\ln(\rho)/R$, where $\rho \in (0,1)$ is a random number and $R = \Sigma_i r_i$ is the total cumulative rate (*26*). Each kMC trajectory was performed for up to 100 steps; if barriers become too low ($E^{\ddagger} \ll k_B T$), this is taken as an implication of CNT failure, and the simulation is terminated. At each kMC step, the selected/mew configuration is first annealed at the given T for ~20 ps to ensure its stability. If the structure is not stable (broken bonds), it is considered as another instance of CNT failure and the simulation is terminated. The flowchart of the algorithm is provided in section S5.

LCBOP correction

Bond-order empirical potentials such as the adaptive intermolecular reactive empirical bond order (AIREBO) potential and LCBOP are commonly used to model carbon nanoforms (*48*) and are expected to capture defects energetics and strain effects as long as the sp^2 hybridization is maintained. However, the energies of defect configurations from these potentials can deviate significantly from those obtained by DFTB. This poses a problem for accurate estimates of barriers, and thereby, time scales for such processes as errors are exponentiated. Thus, the LCBOP-computed values were corrected through selective regression, as explained in section S3. The barriers are then obtained by assuming the same BEP relationship between ΔH and $H^{\ddagger}$ as in Fig. 2A.

Coarse-grained model

The basic coarse-grained model (*10*) represents a CNT by a chain of beads, whose configuration is controlled by harmonic bonds and three-bead harmonic angular potential term. The bond and angular spring constants are fitted to represent a (5,5) nanotube, with a single bead representing a CNT segment of ≃20 carbon atoms. The nonbonded (intertube) interactions are represented by a Lennard-Jones potential with a shifted (from the center axis to the CNT wall) argument. In addition, a granular-type interaction potential (*49*) is used to introduce interface friction. Further details of the coarse-grained model as implemented in LAMMPS are provided in section S6.

Coarse-grained simulations

The tensile cyclic loading tests of CNT bundles are simulated with LAMMPS (*47*). An example script is provided in section S7. Note that for $f = 0$, the bundle is only held together by capillary forces and any load exceeding the very low capillary stress ~0.45 GPa will cause the bundle to fail quickly. On the other hand, large f results in the interface strength comparable or surpassing the intrinsic tube strength, which has not yet been achieved experimentally, and may even be far-fetched to realize. These considerations led us to use as an appropriate value of $f = 0.01$ nN/Å and $L = 100$ nm for the bulk CNT bundle, which correspond to a strength of ≃12 GPa (*10*). For the bundle bulk, both load- and displacement-control modes are realized. The former is achieved by ramping up the longitudinal pressure in the simulation box up to desired value σ_0, while the latter is achieved by increasing the longitudinal simulation box size at a constant rate of 0.1 Å/ps. Typical σ-ε curves under cyclic loading are shown in Fig. 4 (A and B). The finite-width bundle of diameter ≃7.5 nm comprises 110 CNTs (composed of more than ~5×10^5 beads; 55 CNTs in the cross section), with periodic boundary conditions applied axially and corresponding simulation box length of 2 μm. The CNT lengths are normally distributed, with mean $\langle L \rangle = 1$ μm and SD of 0.3 μm.

SUPPLEMENTARY MATERIALS

Supplementary material for this article is available at https://science.org/doi/10.1126/sciadv.abj6996

REFERENCES AND NOTES

1. S. Suresh, *Fatigue of Materials* (Cambridge Univ. Press, 2012).
2. I. V. Vlassiouk, Y. Stehle, P. R. Pudasaini, R. R. Unocic, P. D. Rack, A. P. Baddorf, I. N. Ivanov, N. V. Lavrik, F. List, N. Gupta, K. V. Bets, B. I. Yakobson, S. N. Smirnov, Evolutionary selection growth of two-dimensional materials on polycrystalline substrates. *Nat. Mater.* **17**, 318–322 (2018).
3. Y. Bai, H. Yue, J. Wang, B. Shen, S. Sun, S. Wang, H. Wang, X. Li, Z. Xu, R. Zhang, F. Wei, Super-durable ultralong carbon nanotubes. *Science* **369**, 1104–1106 (2020).
4. T. Cui, S. Mukherjee, P. M. Sudeep, G. Colas, F. Najafi, J. Tam, P. M. Ajayan, C. V. Singh, Y. Sun, T. Filleter, Fatigue of graphene. *Nat. Mater.* **19**, 405–411 (2020).
5. T. Cui, K. Yip, A. Hassan, G. Wang, X. Liu, Y. Sun, T. Filleter, Graphene fatigue through van der Waals interactions. *Sci. Adv.* **6**, eabb1335 (2020).
6. M. D. Sangid, The physics of fatigue crack initiation. *Int. J. Fatigue* **57**, 58–72 (2013).
7. B. I. Yakobson, C. J. Brabec, J. Bernholc, Nanomechanics of carbon tubes: Instabilities beyond linear response. *Phys. Rev. Lett.* **76**, 2511–2514 (1996).
8. T. Dumitrica, M. Hua, B. I. Yakobson, Symmetry-, time-, and temperature-dependent strength of carbon nanotubes. *Proc. Natl. Acad. Sci. U.S.A.* **103**, 6105–6109 (2006).
9. A. Takakura, K. Beppu, T. Nishihara, A. Fukui, T. Kozeki, T. Namazu, Y. Miyauchi, K. Itami, Strength of carbon nanotubes depends on their chemical structures. *Nat. Commun.* **10**, 3040 (2019).
10. N. Gupta, J. M. Alred, E. S. Penev, B. I. Yakobson, Universal strength scaling in carbon nanotube bundles with frictional load transfer. *ACS Nano* **15**, 1342–1350 (2021).
11. J. J. Vilatela, J. A. Elliott, A. H. Windle, A model for the strength of yarn-like carbon nanotube fibers. *ACS Nano* **5**, 1921–1927 (2011).
12. D. E. Tsentalovich, R. J. Headrick, F. Mirri, J. Hao, N. Behabtu, C. C. Young, M. Pasquali, Influence of carbon nanotube characteristics on macroscopic fiber properties. *ACS Appl. Mater. Interfaces* **9**, 36189–36198 (2017).
13. E. Yang, Z. Xu, M. Baniasadi, S. Moreno, H. Yi, J. Di, R. Baughman, M. Minary-Jolandan, Tensile fatigue behavior of single carbon nanotube yarns. *J. Mater. Sci.* **53**, 11426–11432 (2018).
14. M. Elstner, D. Porezag, G. Jungnickel, J. Elsner, M. Haugk, T. Frauenheim, S. Suhai, G. Seifert, Self-consistent-charge density-functional tight-binding method for simulations of complex materials properties. *Phys. Rev. B* **58**, 7260–7268 (1998).
15. J. H. Los, A. Fasolino, Intrinsic long-range bond-order potential for carbon: Performance in Monte Carlo simulations of graphitization. *Phys. Rev. B* **68**, 024107 (2003).

16. M. B. Nardelli, B. I. Yakobson, J. Bernholc, Brittle and ductile behavior in carbon nanotubes. *Phys. Rev. Lett.* **81**, 4656–4659 (1998).
17. M. Buongiorno Nardelli, B. I. Yakobson, J. Bernholc, Mechanism of strain release in carbon nanotubes. *Phys. Rev. B* **57**, R4277–R4280 (1998).
18. T. Dumitrică, T. Belytschko, B. I. Yakobson, Bond-breaking bifurcation states in carbon nanotube fracture. *J. Chem. Phys.* **118**, 9485–9488 (2003).
19. S. N. Zhurkov, Kinetic concept of the strength of solids. *Int. J. Fract.* **26**, 295–307 (1984).
20. A. C. Hansen, J. Baker-Jarvis, A rate dependent kinetic theory of fracture for polymers. *Int. J. Fract.* **44**, 221–231 (1990).
21. T. Xiao, Y. Ren, K. Liao, A kinetic model for time-dependent fracture of carbon nanotubes. *Nano Lett.* **4**, 1139–1142 (2004).
22. B. I. Yakobson, Mechanical relaxation and "intramolecular plasticity" in carbon nanotubes. *Appl. Phys. Lett.* **72**, 918–920 (1998).
23. P. G. Collins, in *Oxford Handbook of Nanoscience and Technology*, A. V. Narlikar, Y. Y. Fu, Eds. (Oxford Univ. Press, 2010), vol. 2.
24. G. G. Samsonidze, G. G. Samsonidze, B. I. Yakobson, Energetics of Stone–Wales defects in deformations of monoatomic hexagonal layers. *Comput. Mater. Sci.* **23**, 62–72 (2002).
25. B. I. Yakobson, G. Samsonidze, G. G. Samsonidze, Atomistic theory of mechanical relaxation in fullerene nanotubes. *Carbon* **38**, 1675–1680 (2000).
26. A. F. Voter, in *Radiation Effects in Solids*, K. E. Sickafus, E. A. Kotomin, B. P. Uberuaga, Eds. (Nato Science Series, Springer Netherlands, 2007), pp. 1–23.
27. K. A. Fichthorn, W. H. Weinberg, Theoretical foundations of dynamical Monte Carlo simulations. *J. Chem. Phys.* **95**, 1090–1096 (1991).
28. E. S. Penev, K. V. Bets, N. Gupta, B. I. Yakobson, Transient kinetic selectivity in nanotubes growth on solid Co–W catalyst. *Nano Lett.* **18**, 5288–5293 (2018).
29. J. Kotakoski, A. V. Krasheninnikov, K. Nordlund, Kinetic Monte Carlo simulations of the response of carbon nanotubes to electron irradiation. *J. Comput. Theor. Nanosci.* **4**, 1153–1159 (2007).
30. Y. Wang, P. Verma, X. Jin, D. G. Truhlar, X. He, Revised M06 density functional for main-group and transition-metal chemistry. *Proc. Natl. Acad. Sci. U.S.A.* **115**, 10257–10262 (2018).
31. J. Huang, S. Chen, Z. Wang, K. Kempa, Y. Wang, S. Jo, G. Chen, M. Dresselhaus, Z. Ren, Superplastic carbon nanotubes. *Nature* **439**, 281 (2006).
32. N. Shadmi, A. Kremen, Y. Frenkel, Z. J. Lapin, L. D. Machado, S. B. Legoas, O. Bitton, K. Rechav, R. Popovitz-Biro, D. S. Galvão, A. Jorio, L. Novotny, B. Kalisky, E. Joselevich, Defect-free carbon nanotube coils. *Nano Lett.* **16**, 2152–2158 (2016).
33. F. Xu, Z. Xu, B. I. Yakobson, Site-percolation threshold of carbon nanotube fibers—Fast inspection of percolation with Markov stochastic theory. *Phys. A* **407**, 341–349 (2014).
34. F. Alonso-Marroquín, H. J. Herrmann, Ratcheting of granular materials. *Phys. Rev. Lett.* **92**, 054301 (2004).
35. R. S. Rajpurohit, P. Mishra, N. C. S. Srinivas, S. R. Singh, V. Singh, Ratcheting fatigue behaviour of zircaloy-2 at 300 °C. *Met. Mater. Int.* **27**, 3143–3154 (2021).
36. S. Wang, Z. Xu, On the elastic rod models for mechanical tests of one-dimensional nanostructures under transverse loads. *J. Appl. Phys.* **128**, 164303 (2020).
37. K. Hemalatha, A. S. Prakash, K. Guruprakash, M. Jayakumar, TiO_2 coated carbon nanotubes for electrochemical energy storage. *J. Mater. Chem. A* **2**, 1757–1766 (2014).
38. M. R. Falvo, G. Clary, R. Taylor II, V. Chi, F. Brooks, S. Washburn, R. Superfine, Bending and buckling of carbon nanotubes under large strain. *Nature* **389**, 582–584 (1997).
39. H. E. Misak, R. Asmatulu, V. Sabelkin, S. Mall, P. E. Kladitis, Tension–tension fatigue behavior of carbon nanotube wires. *Carbon* **52**, 225–231 (2013).
40. X. Wei, Z. Meng, L. Ruiz, W. Xia, C. Lee, J. W. Kysar, J. C. Hone, S. Keten, H. D. Espinosa, Recoverable slippage mechanism in multilayer graphene leads to repeatable energy dissipation. *ACS Nano* **10**, 1820–1828 (2016).
41. W. Xia, L. Ruiz, N. M. Pugno, S. Keten, Critical length scales and strain localization govern the mechanical performance of multi-layer graphene assemblies. *Nanoscale* **8**, 6456–6462 (2016).
42. W. Xu, Y. Chen, H. Zhan, J. N. Wang, High-strength carbon nanotube film from improving alignment and densification. *Nano Lett.* **16**, 946–952 (2016).
43. B. Aradi, B. Hourahine, T. Frauenheim, DFTB+, a sparse matrix-based implementation of the DFTB method. *J. Phys. Chem. A* **111**, 5678–5684 (2007).
44. G. Henkelman, B. P. Uberuaga, H. Jónsson, A climbing image nudged elastic band method for finding saddle points and minimum energy paths. *J. Chem. Phys.* **113**, 9901–9904 (2000).
45. A. H. Larsen, J. J. Mortensen, J. Blomqvist, I. E. Castelli, R. Christensen, M. Dulak, J. Friis, M. N. Groves, B. Hammer, C. Hargus, E. D. Hermes, P. C. Jennings, P. B. Jensen, J. Kermode, J. R. Kitchin, E. L. Kolsbjerg, J. Kubal, K. Kaasbjerg, S. Lysgaard, J. B. Maronsson, T. Maxson, T. Olsen, L. Pastewka, A. Peterson, C. Rostgaard, J. Schiøtz, O. Schütt, M. Strange, K. S. Thygesen, T. Vegge, L. Vilhelmsen, M. Walter, Z. Zeng, K. W. Jacobsen, The atomic simulation environment—A Python library for working with atoms. *J. Phys. Condens. Matter* **29**, 273002 (2017).
46. M. Liu, V. I. Artyukhov, B. I. Yakobson, Mechanochemistry of one-dimensional boron: Structural and electronic transitions. *J. Am. Chem. Soc.* **139**, 2111–2117 (2017).
47. S. J. Plimpton, Fast parallel algorithms for short-range molecular dynamics. *J. Comput. Phys.* **117**, 1–19 (1995).
48. S. Thomas, K. M. Ajith, S. Uck Lee, M. C. Valsakumar, Assessment of the mechanical properties of monolayer graphene using the energy and strain-fluctuation methods. *RSC Adv.* **8**, 27283–27292 (2018).
49. L. E. Silbert, D. Ertaş, G. S. Grest, T. C. Halsey, D. Levine, S. J. Plimpton, Granular flow down an inclined plane: Bagnold scaling and rheology. *Phys. Rev. E* **64**, 051302 (2001).

Acknowledgments
Funding: This work was supported by Air Force Office of Scientific Research (AFOSR) grant FA9550-17-1-0262 and by the Welch Foundation grant C-1590. Computer resources were provided by XSEDE, which is supported by NSF grant ACI-1548562, under allocation TG-DMR100029, and the NOTS cluster at Rice University acquired with funds from NSF grant CNS-1338099. **Author contributions:** Conceptualization: B.I.Y. Methodology: N.G., E.S.P., and B.I.Y. Investigation: N.G. and E.S.P. Visualization: N.G. and E.S.P. Supervision: B.I.Y. Writing—original draft: N.G., E.S.P., and B.I.Y. Writing—review and editing: N.G., E.S.P., and B.I.Y. **Competing interests:** The authors declare that they have no competing interests. **Data and materials availability:** All data needed to evaluate the conclusions in the paper are present in the paper and/or the Supplementary Materials.

Submitted 26 May 2021
Accepted 9 November 2021
Published 22 December 2021
10.1126/sciadv.abj6996